

Article

NO Oxidation on Lanthanum-Doped Ceria Nanoparticles with Controlled Morphology

Susana Fernández-García ¹, Miguel Tinoco ^{2,*}, Ana Belén Hungría ¹, Xiaowei Chen ¹, José Juan Calvino ¹, Juan Carlos Martínez-Munuera ³, Javier Giménez-Mañogil ³ and Avelina García-García ^{3,*}

- ¹ Departamento de Ciencia de los Materiales, Ingeniería Metalúrgica y Química Inorgánica, Facultad de Ciencias, Universidad de Cádiz, Campus Río San Pedro, 11510 Cádiz, Spain; susana.fernandezgarcia@gm.uca.es (S.F.-G.); ana.hungria@uca.es (A.B.H.); xiaowei.chen@uca.es (X.C.); jose.calvino@uca.es (J.J.C.)
- ² Departamento de Química Inorgánica, Facultad de Ciencias Químicas, Universidad Complutense de Madrid, 28020 Madrid, Spain
- ³ Departamento de Química Inorgánica e Instituto Universitario de Materiales, Universidad de Alicante, Carretera de San Vicente s/n, 03690 San Vicente del Raspeig, Spain; jc.martinez@ua.es (J.C.M.-M.); javier.gimenez@ua.es (J.G.-M.)
- * Correspondence: mitinoco@ucm.es (M.T.); a.garcia@ua.es (A.G.-G.); Tel.: +34-913948502 (M.T.); +34-965909410 (A.G.-G.)

Abstract: The present work aims to assess the impact of morphology and reducibility on lanthanum-doped ceria nanocatalysts with controlled morphology on the NO oxidation reaction. Specifically, samples were prepared using a hydrothermal method incorporating lanthanum at varying molar concentrations (0, 5, 10, and 15 mol.%) into ceria with a controlled morphology (nanocubes and nanorods). The structural, compositional, and redox characterization of these catalysts has been performed via scanning transmission electron microscopy (STEM), X-ray diffraction (XRD), X-ray energy dispersive spectroscopy (X-EDS), inductively coupled plasma (ICP), hydrogen temperature-programmed reduction (H₂-TPR), and oxygen storage capacity (OSC). NO oxidation catalytic tests were conducted, and the results were compared with estimated curves (obtained by considering the proportions of the corresponding components), which revealed the presence of a synergistic effect between lanthanum and ceria. The degree of enhancement was found to depend on both the morphology and the amount of lanthanum incorporated into CeO₂. These findings may facilitate the optimization of features concerning ceria-based nanocatalysts for the removal of NO_x emissions from exhaust gases.

Keywords: lanthanum; ceria; nanocubes; nanorods; NO oxidation



Citation: Fernández-García, S.; Tinoco, M.; Hungría, A.B.; Chen, X.; Calvino, J.J.; Martínez-Munuera, J.C.; Giménez-Mañogil, J.; García-García, A. NO Oxidation on Lanthanum-Doped Ceria Nanoparticles with Controlled Morphology. *Catalysts* **2023**, *13*, 894. <https://doi.org/10.3390/catal13050894>

Academic Editors: Diego Luna, Sergio Carrasco and Rebeca Martínez-Haya

Received: 12 April 2023
Revised: 5 May 2023
Accepted: 11 May 2023
Published: 15 May 2023



Copyright: © 2023 by the authors. Licensee MDPI, Basel, Switzerland. This article is an open access article distributed under the terms and conditions of the Creative Commons Attribution (CC BY) license (<https://creativecommons.org/licenses/by/4.0/>).

1. Introduction

The adverse environmental impact of nitrogen oxides (NO_x) generated by the combustion of fossil fuels (e.g., coal-fired plants, industrial boilers, and vehicles powered by internal combustion engines) is widely recognized, leading to harmful effects such as acid rain, photochemical “smog”, and ozone depletion [1,2]. To mitigate these effects, there is an urgent need to develop effective and sustainable strategies to control NO_x emissions [3]. Focusing on automotive combustion engines, NO_x is recognized as a major contributor to air pollution, causing several health issues, such as neurological diseases, emphysema, and bronchitis [4,5]. Diesel engines emit a higher quantity of NO_x pollutants (referred to as NO and NO₂, but mainly NO) as a result of lean burn conditions, which are more efficient than those of stoichiometric combustion. Increasing the ratio of NO₂/NO_x in the exhaust gas of lean-burning vehicles improves the low-temperature activity of the so-called fast selective catalytic reduction (2NH₃ + NO + NO₂ → 2N₂ + 3H₂O) [6] and the adsorption performance of the storage reduction (NSR) catalyst and accelerates the continuous regeneration of the

diesel particulate filter. As NO_2 is a more powerful oxidant gas than O_2 and NO [7,8], the selective catalytic oxidation of NO to NO_2 is considered a critical step in the development of the aforementioned strategies [9–11]. In this context, the design of catalysts with high activity, selectivity, and stability capable of oxidizing NO to NO_2 is of particular interest [5].

Catalysts based on precious metals (Pt, Pd, Ru, Rh) have been traditionally used for NO oxidation to NO_2 owing to their outstanding catalytic performances [12,13]. However, their scarcity and high price limit their widespread use as catalysts [14]. Therefore, exploring and developing noble-metal-free alternatives can be considered a possible avenue to moderate the prices of catalysts devoted to this chemical reaction [2,15]. Hence, the use of ceria and related materials for environmental catalysis has attracted much attention in recent years. As it is well known, CeO_2 possesses excellent redox properties due to its facile redox pair state of cerium ($\text{Ce}^{4+}/\text{Ce}^{3+}$) and, consequently, the concomitant creation of oxygen vacancies [16].

Previous studies have focused on generating controlled-morphology nanoparticles with well-defined facets to improve the catalytic activity of ceria-based materials. The approach of using controlled morphology can be interpreted from different views and by using several routes of preparation. In this line, Zhu et al. [17] reported the regulation of different morphologies for CeO_2 by a hard template method and the successful application to the oxidation of toluene at low temperature. CeO_2 -nanoparticles with more oxygen vacancies exhibited the highest efficiency, improving the toluene oxidation performance with regard to CeO_2 with a three-dimensional ordered microporous structure and a CeO_2 -bulk sample. Controlled size and morphology play crucial roles in the physical and chemical properties of CeO_2 . In fact, ceria with different exposed crystalline planes, such as {111} and {110} facets for nanorods, {100} surfaces for nanocubes, and {111} facets for nano-octahedra, have been used in catalytic activity for CO oxidation, soot combustion, NO reduction, glycerol oxidation, methanol synthesis, etc. [18–22]. For example, several authors found that the facets exposed by nanorods are more active for CO oxidation than other nanofacets [23–25]. Furthermore, CeO_2 nanorods and nanocubes have been demonstrated to have higher oxygen storage capacity than octahedra [26]. In conclusion, controlling the crystalline planes in ceria nanoparticles is an effective way to improve their redox characteristics and catalytic activity.

Another alternative to enhance the redox properties and catalytic performance of ceria is to encourage the proliferation of new oxygen vacancies either by doping with transition metals (e.g., Mn, Cu, Ag) yielding differently modified ceria or by the incorporation of other elements into its crystalline structure. Regarding the first case, Di Sarli et al. [27] reported some Ag-ceria catalysts with significantly enhanced silver–ceria interface, where highly reactive oxygen species were produced yielding an outstanding catalytic activity towards diesel soot combustion during regeneration of a coated DPF. On the other hand, previous studies have demonstrated that doping CeO_2 with tetravalent transition metal cations such as Ti^{4+} and Zr^{4+} [28,29], or other trivalent rare earth cations such as Tb^{3+} , Gd^{3+} , Eu^{3+} , La^{3+} , and Pr^{3+} [30–33], increases both oxygen mobility and the number of oxygen vacancies within the structure, which in turn is reflected in a considerable improvement of its redox properties, in most cases. La^{3+} possesses an ionic radius similar to Ce^{4+} (116 and 97 pm, respectively), which results in its facile incorporation into the crystalline lattice of cerium oxide. Moreover, La addition into ceria decreases the sintering effect of nanoparticles at high temperatures [34]. The incorporation of lanthanum into controlled-morphology ceria nanoparticles has recently attracted scientific attention due to the advantages mentioned before [35–38]. For example, Xia et al. [37] have recently published the synthesis of La-, Y-, or Sm-doped ceria nanorods with dopant molar concentrations ranging between 0 and 30%. An excellent photocatalytic performance of the samples with a molar ratio of 10% was obtained. Sartoretto et al. [38] have reported the synthesis and characterization of ceria catalysts modified with La and Nd with concentrations of 10, 25, and 50 at.% and their performance in oxidation reactions such as CO, NO, and soot oxidation. Their results suggest that large additions of La and Nd do not significantly affect the catalytic behavior

of the nanoparticles in NO oxidation, and only the sample with 10% lanthanum, whose nanoparticles possess a nanocube and nanowire morphology, exhibits a slightly higher catalytic conversion compared to pure ceria. The authors attribute this effect to the limited influence of the incorporation of the dopant elements on the reducibility of their nanoparticles. Nevertheless, to the best of our knowledge, the influence of morphological aspects and composition homogeneity in both redox and catalytic responses for NO oxidation of La-doped ceria has been not fully explored.

In the present work, the incorporation of lanthanum into ceria nanocubes synthesized under hydrothermal conditions was studied. The structure and redox properties of all samples were assessed to gain insights into the NO oxidation reaction. In parallel, lanthanum hydroxide nanorods were prepared to measure and compare their NO oxidation catalytic activity with that of both pure and La-doped ceria nanoparticles. These results may provide a better understanding of the effect and relevance of the different parameters affecting the catalytic activity of lanthanum-doped ceria nanoparticles for NO oxidation. In summary, the impact of composition and morphology on the redox behavior (including reducibility and OSC properties) of La-doped ceria nanocatalysts synthesized using a soft (hydrothermal) method to achieve controlled morphology was studied. We examined the correlations between these properties and their corresponding performances in the NO oxidation reaction, a reaction with significant environmental interest. Our experimental approach was comprehensive and systematic, with the goal of establishing critical relationships between La-CeO₂ composition, structure, morphology, and catalytic activity.

2. Results and Discussion

2.1. Structural and Compositional Analysis of the Ce_{1-x}La_xO_{2-δ} Samples

Figure 1 displays representative TEM images of the as-synthesized samples. As shown in these images, all nanoparticles possess a homogeneous cubic morphology in CeO₂ NC, Ce_{0.95}La_{0.05}O_{2-δ} NC, and Ce_{0.90}La_{0.10}O_{2-δ} NC samples, whereas the Ce_{0.85}La_{0.15}O_{2-δ} NC+NR sample is formed by the combination of both nanocubes and nanorods. The particle size of nanocubes varies from 5 to 50 nm in all samples, including Ce_{0.85}La_{0.15}O_{2-δ} NC+NR. On the other hand, nanorods from Ce_{0.85}La_{0.15}O_{2-δ} NC+NR are moderately bent, possibly due to their high aspect ratio: their diameter ranges between 10 and 40 nm, whilst their length spans between 200 nm and 1 μm.

XRD patterns of all the synthesized samples are shown in Figure 2a. As can be confirmed from Figure 2a, all samples possess a face-centered cubic fluorite-like ceria structure (Fm $\bar{3}$ m) [26,39]; no additional reflections are spotted, and thus, no secondary crystalline phases can be identified within the samples. This may suggest that La has been fully incorporated into ceria forming a solid solution [40,41].

Nevertheless, the most intense reflection of the diffractograms of La-modified ceria samples, corresponding to {111} planes, is slightly shifted to lower angles compared to pure ceria. This displacement increases with the lanthanum introduced within the fluorite lattice, following the sequence of $2\theta^{(0)}$ CeO₂ NC (28.50°) > Ce_{0.95}La_{0.05}O_{2-δ} NC (28.40°) = Ce_{0.90}La_{0.10}O_{2-δ} NC (28.40°) > Ce_{0.85}La_{0.15}O_{2-δ} NC+NR (28.35°). Although the ionic radii of La³⁺ and Ce⁴⁺ are similar, this shift can be attributed to the larger radius of lanthanum cations (116 pm) compared to tetravalent cerium (97 pm) [42]. The formation of a solid solution by the incorporation of La into the CeO₂ lattice is confirmed by lattice parameter calculations based on the {111} diffraction of all diagrams [31,34,43–48]. Moreover, the lattice distortion due to the incorporation of lanthanum can facilitate the creation of additional oxygen vacancies beyond those intrinsically necessary to maintain the principle of neutrality of the mixed oxide [30,31]. As can be seen in Table 1, the values of the lattice parameter increase slightly with the molar concentration of La.

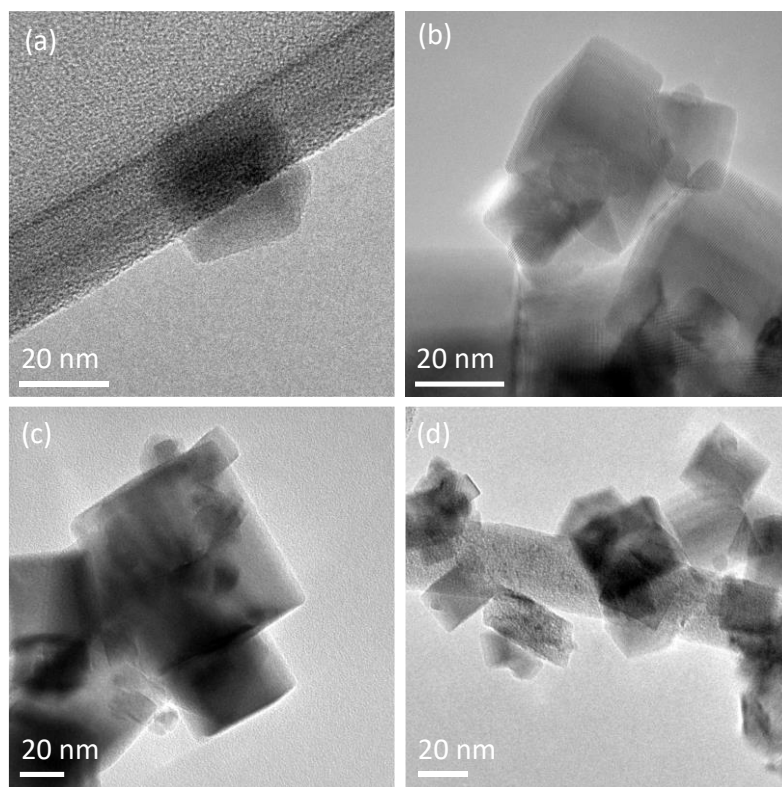


Figure 1. TEM images of (a) CeO₂ NC, (b) Ce_{0.95}La_{0.05}O_{2-δ} NC, (c) Ce_{0.90}La_{0.10}O_{2-δ} NC, and (d) Ce_{0.85}La_{0.15}O_{2-δ} NC+NR.

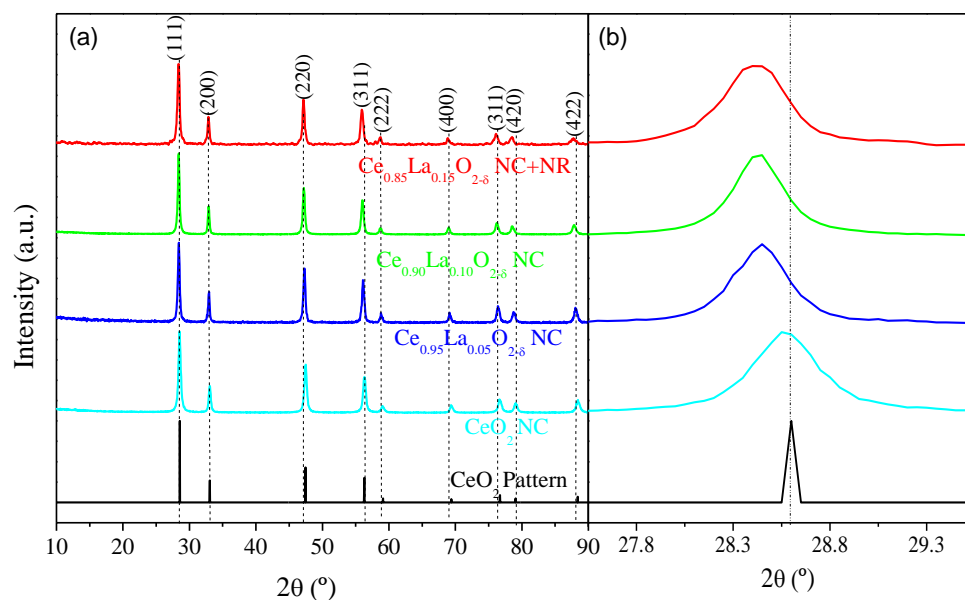


Figure 2. (a) XRD diffractograms of La-modified ceria samples at different concentration mol.% of lanthanum, compared with ceria nanocube reference and CeO₂ bulk pattern (Inorganic Crystal Structure Database (ICSD)). (b) Zoom on the {111} reflection of all samples, demonstrating the slight shift to smaller angles.

Table 1. Morphological, compositional, and structural characteristics of $Ce_{1-x}La_xO_{2-\delta}$ nanoshapes.

Samples	Morphology	Nominal mol.% of La	mol.% of La by ICP	Lattice Parameter (Å) ^a	τ_{Scherrer} (nm) ^b	BET Surface Areas (m ² /g)
CeO ₂ NC	Nanocubes	-	-	5.413	21	38
Ce _{0.95} La _{0.05} O _{2-δ} NC	Nanocubes	5	4.4	5.437	26	23
Ce _{0.90} La _{0.10} O _{2-δ} NC	Nanocubes	10	9.7	5.440	28	25
Ce _{0.85} La _{0.15} O _{2-δ} NC+NR	Nanocubes + Nanorods	15	14.4	5.443	29	29

^a Values obtained considering the Bragg law. ^b Results calculated by Scherrer equation using the {111} reflection of ceria from XRD data in all samples.

On the other hand, the average crystal sizes of all the nanocatalysts have been estimated by using the Scherrer equation, measuring the FWHM (full width, half maximum) of the {111} diffraction reflection. As observed in Table 1, the size of crystallites increases with the amount of lanthanum introduced, but the rate of increase gradually slows down with lanthanum content.

To assess the crystallography of the nanocubes in each sample, high-resolution transmission electron microscopy (HRTEM) images were acquired. Figure S1 depicts representative HRTEM images of each catalyst. The reflections observed in the digital diffraction patterns (DDPs), obtained from the white enclosed regions, can be accurately indexed to a CeO₂ crystalline phase, as expected. In particular, 2.7 Å distances perpendicular to each other and 1.9 Å distances generating a 45° angle with the previous reflections were measured, which correspond to {200} and {220} ceria family planes, respectively, in a crystal viewed along a [100] zone axis (Figure S1a–c). On the other hand, 2.7 Å and 3.1 Å distances forming 55° angles between each other can be indexed to {200} and {111} family planes, respectively, in a ceria crystal oriented along a [110] zone axis (Figure S1d).

On the other hand, the specific surface areas of all samples were determined by Brunauer–Emmett–Teller (BET) method (See Table 1). La-doped ceria nanocatalysts present surface values similar between them (23, 25, and 29 m²/g, respectively). However, the CeO₂ nanocube sample presents the highest surface area (38 m²/g) among all the samples, which agrees with the smallest particle size estimated by the Scherrer equation.

Table 1 also shows the actual molar concentration of La cations in Ce_{0.95}La_{0.05}O_{2- δ} NC, Ce_{0.90}La_{0.10}O_{2- δ} NC, and Ce_{0.85}La_{0.15}O_{2- δ} NC+NR samples, estimated by ICP. The as-obtained results were 4.4, 9.7, and 14.4 mol.%, respectively, which are very close to the expected concentrations.

In order to analyze the local lanthanum composition in these nanocatalysts, X-EDS spectra were acquired at different positions on the samples. However, due to the proximity of lanthanum and cerium signals in X-EDS, and the low amount of lanthanum in samples Ce_{0.95}La_{0.05}O_{2- δ} and Ce_{0.90}La_{0.10}O_{2- δ} , the lanthanum lines could not be clearly distinguished from the more intense cerium signals. Therefore, the quantitative X-EDS results obtained from these samples differed from the expected ones and disagreed with quantitative EELS results that were previously published elsewhere [47]. These EELS analyses confirmed that lanthanum was homogeneously distributed within the samples, and the amount of lanthanum corresponded to 5 and 10 mol.%, respectively, as expected. Nevertheless, Figure 3 displays a representative HAADF-STEM image and X-EDS spectra of sample Ce_{0.85}La_{0.15}O_{2- δ} NC+NR, which contains enough lanthanum to be accurately quantified by X-EDS. As can be seen in Figure 3a, two morphologies can be distinguished: nanocubes and nanorods. X-EDS spectra were recorded at various positions on nanorods (Figure 3b, locations 1 and 3) and on different nanocubes (Figure 3b, positions 2 and 4). Quantitative results evidence that nanorods are richer in lanthanum than nanocubes. In the former, the average La content amounts to 19 ± 5 at.%, whereas the value obtained for nanocubes is just 11 ± 2 at.%. Additionally, these results verify that the distribution

of lanthanum along the nanorods is not homogeneous (19 at.% vs. 14 at.% at positions 1 and 3 from Figure 3b). To examine the morphology of pure lanthanum oxide nanoparticles under the hydrothermal conditions employed in this study, another catalyst was prepared using only lanthanum nitrate hexahydrate as a precursor. Therefore, a $\text{La}(\text{OH})_3$ nanorod sample was synthesized under the same hydrothermal conditions to confirm that crystallites rich in lanthanum tend to form a rod-shaped morphology with a hexagonal structure. Figures S2 and S3 contain TEM images and an XRD diagram of this sample, respectively, which consisted of $\text{La}(\text{OH})_3$ nanorods.

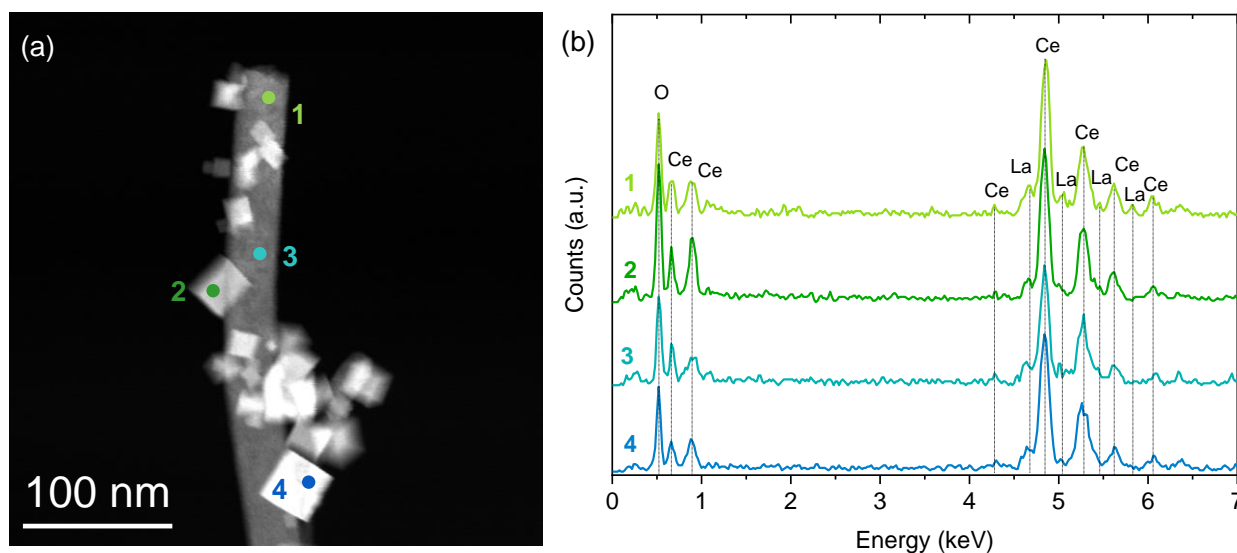


Figure 3. (a) HAADF-STEM image of sample $\text{Ce}_{0.85}\text{La}_{0.15}\text{O}_{2-\delta}$ NC+NR, (b) X-EDS spectra acquired at distinct positions marked with numbers in the image (a). The La/Ce ratios quantified at these exact locations are 19 at.%, 12 at.%, 14 at.%, and 9 at.% at positions 1, 2, 3, and 4, respectively.

These results indicate that the maximum concentration of lanthanum that can be incorporated into the ceria lattice while maintaining a nanocube morphology is 10 mol.% under hydrothermal conditions. Several authors have reported that the maximum solubility of La^{3+} in ceria, forming a solid solution without taking into consideration morphological aspects by the coprecipitation method, is about 50% mol. [43]. Loche et al. [40] indicated that the upper limit to the incorporation of La into ceria nanocubes prepared with a surfactant-assisted hydro-solvothermal synthesis is close to 7.5 mol.%, corroborated by XRD and transmission electron microscopy. Recently, Trindade et al. [35] obtained La/Ce mixed oxide nanorods and nanocubes by hydrothermal synthesis by modifying temperature conditions. Structural analyses by HREM and XRD confirmed that the maximum concentration of lanthanum that can be introduced into ceria while preserving both the fluorite-type structure and a nanocube morphology in all nanoparticles is about 10 mol.%, which agrees with our study.

2.2. Redox Properties

In order to study the redox behavior of pure and lanthanum-doped ceria nanoparticles, H_2 -TPR and OSC analyses have been performed.

2.2.1. H_2 -TPR Experiments

Figure 4 shows the H_2O evolution of all samples through the H_2 -TPR profiles. H_2 -TPR analysis of undoped ceria and La(10 mol.%) -doped ceria nanocubes have been discussed in a previous work [41]. To briefly sum up our previous results, the reduction profile of CeO_2 nanocubes contains a small peak at 527 °C and another wide peak at 830 °C, as also observed in ceria samples made up of nanoparticles without controlled morphologies [49–52]. In the

case of $\text{Ce}_{0.90}\text{La}_{0.10}\text{O}_{2-\delta}$, the reduction peaks occur at lower temperatures than those of pure ceria.

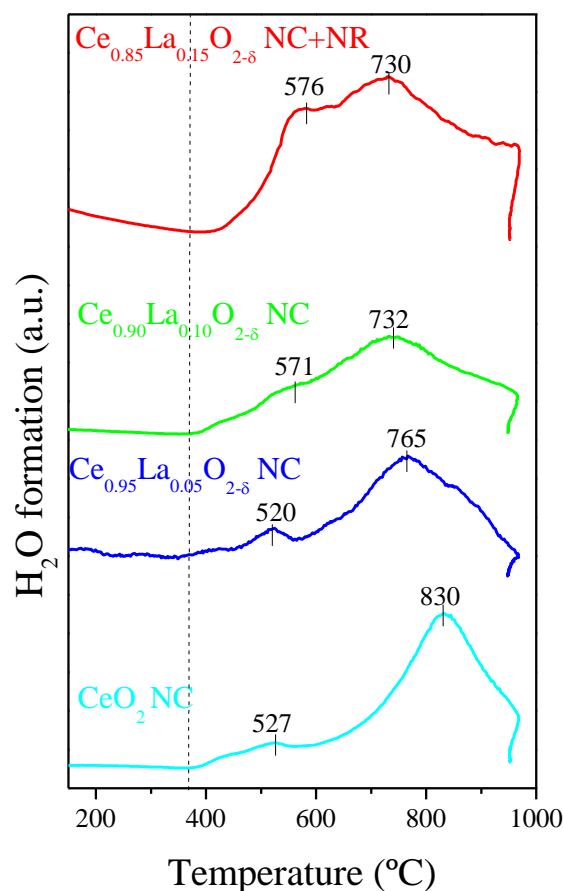


Figure 4. H_2 -TPR profiles of both pure ceria and lanthanum-doped samples.

Figure 4 displays the reduction profile of the reference and lanthanum-doped ceria samples. Two peaks are observed, one occurring at temperatures below $600\text{ }^\circ\text{C}$ and another, more prominent signal appearing above $700\text{ }^\circ\text{C}$. According to previous literature, these can be attributed, respectively, to the surface and bulk reduction of ceria [53,54]. Due to the structural similarities between pure and doped ceria nanocrystals, this assignment can be extrapolated to $\text{Ce}_{0.95}\text{La}_{0.05}\text{O}_{2-\delta}$ NC, $\text{Ce}_{0.90}\text{La}_{0.10}\text{O}_{2-\delta}$ NC, and $\text{Ce}_{0.85}\text{La}_{0.15}\text{O}_{2-\delta}$ NC+NR samples.

In this case, the reduction of samples with lanthanum concentrations of 0, 5, and 10 mol.% starts at similar temperatures (around $370\text{ }^\circ\text{C}$), except for the $\text{Ce}_{0.85}\text{La}_{0.15}\text{O}_{2-\delta}$ NC+NR sample, whose H_2O formation peak initially appears at $420\text{ }^\circ\text{C}$. The first maximum intensity peaks appear at 527, 520, 571, and $576\text{ }^\circ\text{C}$ for CeO_2 NC, $\text{Ce}_{0.95}\text{La}_{0.05}\text{O}_{2-\delta}$ NC, $\text{Ce}_{0.90}\text{La}_{0.10}\text{O}_{2-\delta}$ NC, and $\text{Ce}_{0.85}\text{La}_{0.15}\text{O}_{2-\delta}$ NC+NR catalysts, respectively. Moreover, these surface reduction peaks become more intense and wider as lanthanum content rises, which may suggest the amount of Ce^{3+} generated could be far superior [49,55]. On the other hand, a broad and intense second signal is observed between 730 and $765\text{ }^\circ\text{C}$ for the lanthanum-modified ceria nanocatalysts. The maximum of this reduction peak in the La-modified samples appears at lower temperatures than in pure CeO_2 NC ($830\text{ }^\circ\text{C}$).

These results suggest that the incorporation of increasing amounts of lanthanum into ceria does favor the reduction of the samples at lower temperatures when compared with the reference sample (undoped ceria nanocubes), with the exception of the introduction of 5 mol.% of lanthanum, which does not considerably modify the reducibility of the nanoparticles at low temperature as its surface reduction peaks appears at a temperature similar to that of the pure ceria.

2.2.2. OSC Measurements

OSC measurements of all nanocatalysts are displayed in Figure 5. Lanthanum exclusively presents a trivalent oxidation state, and thus, the observed reducibility during OSC measurements can solely be attributed to the reduction of cerium from Ce^{4+} to Ce^{3+} . As expected, as temperature increases, all samples exhibit increases in their values of oxygen weight loss expressed in mmol of oxygen/mol oxide, and therefore in their reducibility. However, comparing the catalysts, similar reduction behaviors are observed for all samples within the temperature range of 200–350 °C. Consequently, the addition of La into ceria nanocubes does not confer any benefits in terms of reducibility at low temperatures. Furthermore, $\text{Ce}_{0.95}\text{La}_{0.05}\text{O}_{2-\delta}$ NC is the least reducible sample among all tested catalysts until 500 °C, even when compared to undoped ceria. On the other hand, $\text{Ce}_{0.85}\text{La}_{0.15}\text{O}_{2-\delta}$ NC+NR is the most reducible catalyst with 48.3 mmol O/mol oxide at 500 °C. The trend in oxygen weight loss is clearly observed at 700 °C, with 160.7, 128.8, 120.2, and 90.3 mmol O/mol oxide for $\text{Ce}_{0.85}\text{La}_{0.15}\text{O}_{2-\delta}$ NC+NR, $\text{Ce}_{0.90}\text{La}_{0.10}\text{O}_{2-\delta}$ NC, $\text{Ce}_{0.95}\text{La}_{0.05}\text{O}_{2-\delta}$ NC, and CeO_2 NC, respectively. These oxygen release results from ceria agree with the H_2 -TPR results discussed beforehand.

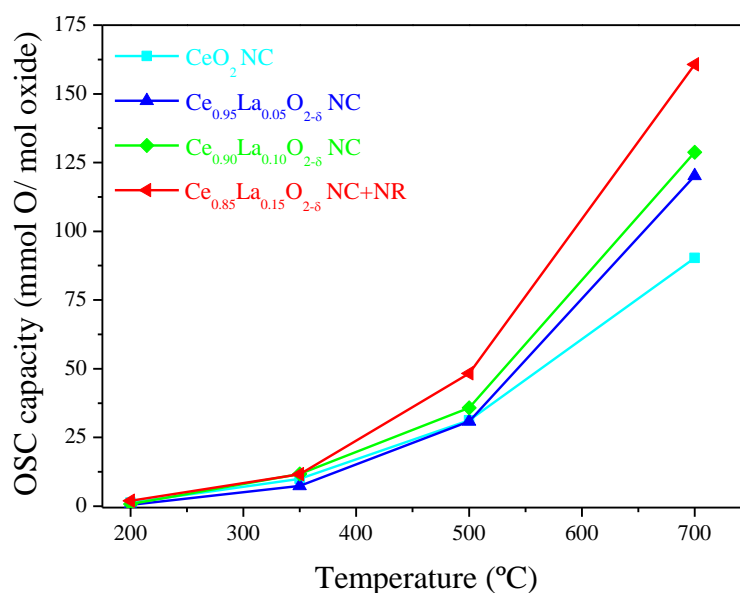


Figure 5. OSC evolution of $\text{Ce}_{1-x}\text{La}_x\text{O}_{2-\delta}$ catalysts.

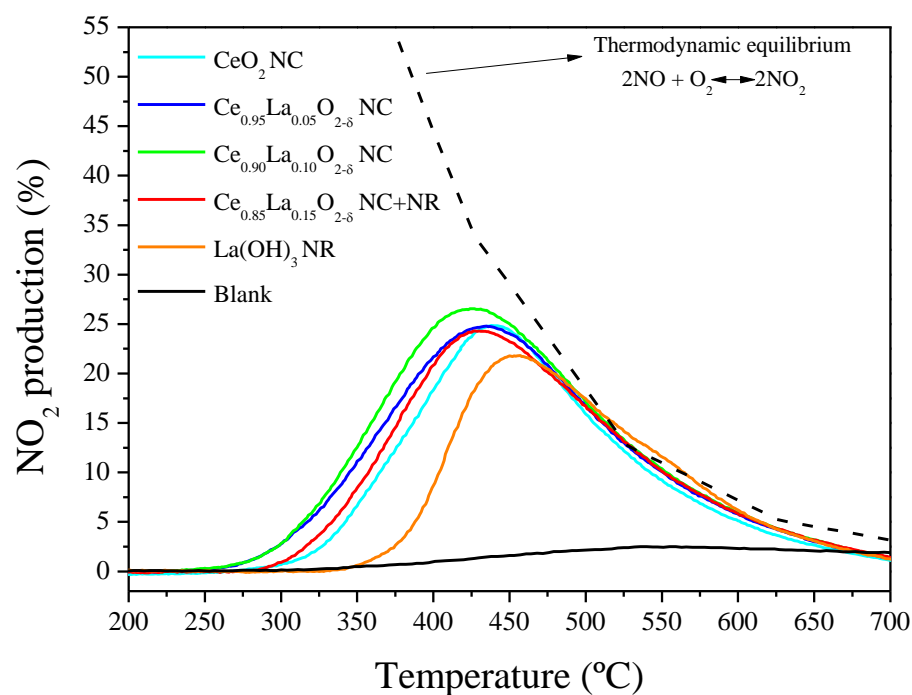
Although cerium is the only reducible element during OSC measurements, it is evident that there is a beneficial effect on reducibility when ceria is doped with La^{3+} , particularly at high temperatures. This is clearly observed in the results presented in Table 2, where cerium total reduction values are listed. These figures have been estimated considering the total amounts of released oxygen and assuming that a negligible amount of Ce^{3+} exists in all samples at room temperature. As expected, the amount of Ce^{3+} increases with reduction temperature in all cases. Likewise, in general, Ce^{3+} percentages increase with lanthanum content, particularly in the case of $\text{Ce}_{0.85}\text{La}_{0.15}\text{O}_{2-\delta}$ NC+NR. Therefore, the incorporation of La^{3+} into the CeO_2 structure not only increases the intrinsic oxygen vacancies related to the substitution of Ce^{4+} with La^{3+} , but also improves the reducibility of Ce^{4+} species, most likely due to the positive effect of intrinsic (La^{3+} -related) oxygen vacancies on the generation and mobility of additional oxygen vacancies linked to the reduction of cerium [41,56].

Table 2. Ce³⁺ proportion on the nanocatalysts at increasing temperatures.

Samples	Ce ³⁺ (%)			
	T _{reduction} (°C)			
	200	350	500	700
CeO ₂ NC	0.2	2.0	6.2	18.1
Ce _{0.95} La _{0.05} O _{2-δ} NC	0.1	1.5	6.4	25.0
Ce _{0.90} La _{0.10} O _{2-δ} NC	0.2	2.6	8.0	28.6
Ce _{0.85} La _{0.15} O _{2-δ} NC+NR	0.4	2.6	11.2	37.3

2.3. Catalytic Activity: Oxidation of NO to NO₂

Since NO oxidation to NO₂ is a key component in several NO_x remediation technologies [57], this reaction has been chosen to evaluate the catalytic performances of the set of synthesized samples. The NO oxidation catalytic activities have been represented as % of NO₂ produced versus temperature in Figure 6.

**Figure 6.** NO₂ production of Ce_{1-x}La_xO_{2-δ} (x: 0, 5, 10, and 15 mol.%) catalysts.

It is deduced that all the samples accelerate the oxidation of NO to NO₂ but to different extents, showing differences both in the onset temperature for the reaction and in the maximum capacity to generate NO₂. In general, the lanthanum-containing samples present higher catalytic activity with considerably lower BET surface areas, regarding the reference sample (undoped CeO₂ NC). On the other hand, La(OH)₃ not only behaves as the least active catalyst regarding NO₂ production capacity but also has an onset temperature which is practically that of the uncatalyzed NO oxidation reaction (black curve), revealing a significant “delay” in promoting the NO oxidation reaction for this solid with regard to the rest of the catalysts.

Since the NO oxidation reaction over ceria-based catalysts is the sum of several steps, including ad-NO_x species formation, their subsequent oxidation, and their final release as NO/NO₂ (this last step depends on several variables, with temperature being of particular importance) [8], the detected NO₂ production should be considered as the combination of parallel processes: NO oxidation–NO₂ storage–corresponding NO₂ desorption (strongly

influenced by thermodynamic limitations, as shown in the corresponding curve for the thermodynamic equilibrium in Figure 6) [58–60]. In this sense, and in an attempt to shed some light on the observed trends of NO_2 production, the corresponding NO_x elimination profiles, as a function of temperature, are depicted in Figure 7. All the samples studied remove NO_x from the gas stream, and this removal is attributed to NO_x chemisorption [58]. Both the population and thermostability of the N-species formed on the sample surface upon NO_x chemisorption (ad- NO_x species) are very dependent on the formulation of the catalysts (as can be seen in Figure 7). By a detailed comparison of both figures (Figures 6 and 7), interesting issues can be inferred: The NO_2 production is prevalent against the generation of thermostable ad- NO_x species (nitrites/nitrates are those expected) for La-Ce samples, which accounts for the shift towards lower temperatures of NO_2 generation. On the contrary, a very large population of ad- NO_x species characterized by a very high thermostability is formed on the $\text{La}(\text{OH})_3$ sample in the course of the reaction. In this particular case, since the desorption/decomposition of NO_x is extended up to 700 °C (with a maximum of desorption at 600 °C), the NO oxidation capacity to NO_2 or the NO_2 emission due to ad- NO_x species decomposition (if any) is unable to be determined due to the NO_2 level decreases following thermodynamics [8].

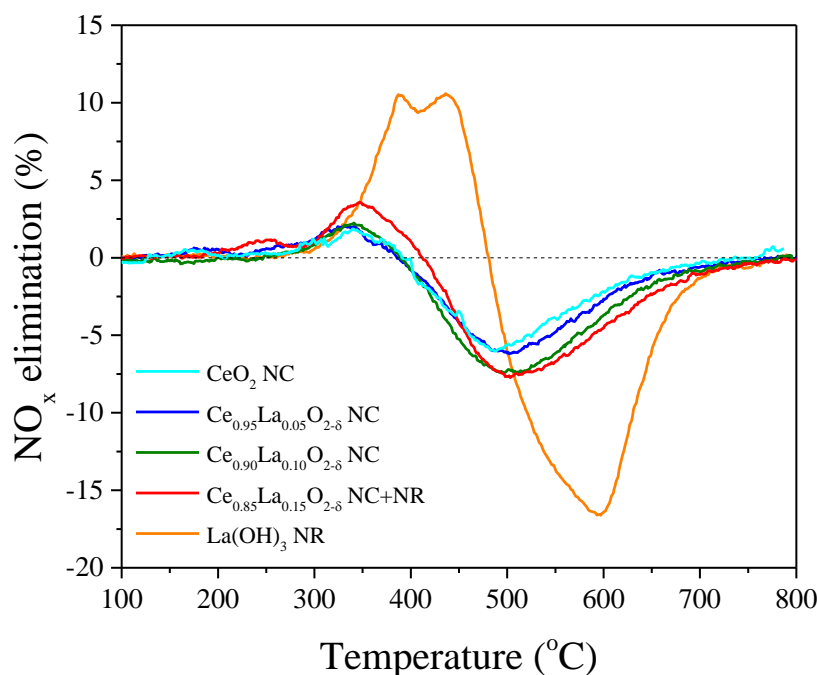


Figure 7. NO_x elimination profiles of $\text{Ce}_{1-x}\text{La}_x\text{O}_{2-\delta}$ (x : 0, 5, 10, and 15 mol.%) catalysts.

$\text{La}(\text{OH})_3$ exhibits a very different behavior, which can be initially explained on the basis of its accentuated basic character. The Lewis basicity of $\text{La}(\text{OH})_3$ is expected to be much higher than that of undoped CeO_2 . Therefore, the trihydroxide compound will present quite strong basic centers where the NO , but mostly NO_2 (being a Lewis acid), will remain “anchored” as thermostable nitrites/nitrates [59]. In addition, $\text{La}(\text{OH})_3$ is likely to exhibit more propensity in adsorbing CO_2 (as an unavoidable contaminant). Indeed, several publications report the trend of this compound to form hydroxycarbonates on its surface because of storage and handling in air [61,62]. This could explain why the “light-off” for its corresponding NO_x elimination curve is a little bit delayed (in the very first stages of the reaction) with regard to that of its counterparts. Nevertheless, once the ad- NO_x species formation is initiated, this population becomes larger and larger up to a temperature as high as 500 °C, proving its very high thermostability.

Interestingly, the introduction of La into the cerium oxide nanocubes concurrently improves both the NO_x chemisorption ability and the NO_2 production capacity following a very smooth and gradual trend along the series (CeO_2 ; $\text{Ce}_{0.95}\text{O}_{0.05}\text{O}_{2-\delta}$ and $\text{Ce}_{0.90}\text{O}_{0.10}\text{O}_{2-\delta}$). In

this set of catalysts, featuring the preservation of the single nanocube morphology, the good features coming from the pure ceria and the pure “lanthana” component seem to be maximized.

In an attempt to go deeper into the analysis of a possible synergism originated by the La-doping onto ceria towards the NO oxidation catalytic activity, Figure S4 illustrates the NO₂ production activities analyzed in this work along with the theoretical curves (dotted lines) that would be obtained for the three mixed oxides adding the curves corresponding to the pure oxides and using the corresponding molar contents in Ce and La as weighting coefficients. These curves (dotted ones in Figure S4) can be considered as a starting point to discuss the synergistic effect caused by the La doping once the intrinsic contribution of the molar proportion of every pure component has been considered.

Interestingly, the maximum synergism seems to be clearly exhibited by Ce_{0.90}O_{0.10}O_{2-δ}, which is the catalyst with the highest La content and unique morphology (NC) (see corresponding green curves). Nevertheless, as discussed in the previous section, this is not the catalyst exhibiting the best redox properties (both quantified by H₂-TPR curves and by OSC measurements). Likewise, Ce_{0.95}O_{0.05}O_{2-δ} NC has a higher activity than the catalyst with the highest lanthanum content, despite its lower OSC. In this sense, the analysis of the mentioned synergism (taking into account these premises) would be much more accurate for Ce_{0.85}O_{0.15}O_{2-δ} because it exhibits mixed morphology (provided by the inherent structures of the bare components). In other words, the effect of the synergism originated by the improvement of redox properties and/or oxygen mobility could be more purely analyzed for this catalyst. Actually, the catalytic activity of Ce_{0.85}O_{0.15}O_{2-δ} shows a relevant synergism (if the corresponding experimental and calculated curves, in red color, are compared), even though this is not as pronounced as that for the Ce_{0.90}O_{0.10}O_{2-δ}, which leads to the assertion of the relevance and influence of the type of morphology/facets exposed by the catalysts for this specific application. Nevertheless, this correlation is not straightforward to establish, and it is possibly influenced by the fact that richer contents in La were detected on the nanorod entities, which in turn seems to favor NO_x chemisorption against NO oxidation. Finally, it is important to remember that Ce_{0.85}O_{0.15}O_{2-δ} presents a higher BET surface area than Ce_{0.95}O_{0.05}O_{2-δ} and Ce_{0.90}O_{0.10}O_{2-δ}, indicating that this parameter is not playing the major role under these experimental conditions, in agreement with the well-referenced literature on this topic [8,59].

The explanation of the improved oxidation capacity of ceria-based catalysts has been envisaged in the open literature from different viewpoints: ease of migration of oxygen vacancies from the bulk to the surface, type of exposed crystal planes, and compositional nanoheterogeneity [29,63]. In fact, from the whole discussion presented, it is suggested that the NO oxidation manifests some surface dependence (even though a simple correlation cannot be assessed under these experimental conditions). Actually, NO oxidation is probably a structure-sensitive reaction [8].

In summary, it can be concluded that a correct balance among redox properties and “suitable” morphologies is highly desirable for the rational design of very active catalysts. In this study, the mixed oxide with formulation Ce_{0.90}O_{0.10}O_{2-δ} seems to exhibit the optimum balance among the best redox properties and oxygen mobility along with the preservation of the unique and most active morphology for this application. This seems to be achieved with a doping of 10% molar concentration of La onto ceria.

The practical significance of the obtained results lies in achieving the control of the final properties of ceria-related catalysts (in the broadest sense) by controlling both the reliable incorporation of elements (amount and type) into the lattice structure of ceria and the nano-morphology by designing rational routes of synthesis. Another important practical aspect is the identification of the relationships among the physicochemical features of the synthesized catalysts (composition, nanostructure, and morphology), their redox properties, and their catalytic activities towards a reaction of environmental interest (such as the NO oxidation reaction).

3. Materials and Methods

3.1. Catalyst Synthesis

Catalysts were prepared using the hydrothermal synthesis conditions described in several publications [41,47]. In particular, lanthanum-doped ceria nanocubes and nanorods were prepared using different molar concentrations (0%, 5%, 10% and 15% mol. La, see Table 1) starting from $\text{La}(\text{NO}_3)_3 \cdot 6\text{H}_2\text{O}$ (99.9%) and $\text{Ce}(\text{NO}_3)_3 \cdot 6\text{H}_2\text{O}$ (99.5%), both salts purchased from Sigma-Aldrich. A mixture of 125 mL of 11.5 M NaOH and 115 mL of a total concentration of 0.050 M corresponding to La and Ce salts was poured into a 300 mL Teflon container. Specifically, 115 mL total volume mixed solutions with molar concentrations of (i) 0.0025 M, (ii) 0.0050 M, and (iii) 0.0075 M in $\text{La}(\text{NO}_3)_3 \cdot 6\text{H}_2\text{O}$ combined with (i) 0.0475 M, (ii) 0.0450 M, and (iii) 0.0425 M in $\text{Ce}(\text{NO}_3)_3 \cdot \text{H}_2\text{O}$ were employed for the preparation of (i) $\text{Ce}_{0.95}\text{La}_{0.05}\text{O}_{2-\delta}$ NC, (ii) $\text{Ce}_{0.90}\text{La}_{0.10}\text{O}_{2-\delta}$ NC, and (iii) $\text{Ce}_{0.85}\text{La}_{0.15}\text{O}_{2-\delta}$ NC+NR samples, respectively. For the synthesis of the CeO_2 NC catalyst, a concentration of 0.050 M in $\text{Ce}(\text{NO}_3)_3 \cdot \text{H}_2\text{O}$ was used. The solution was stirred for 30 min at room temperature. Afterward, the container was introduced into a stainless-steel autoclave, which was heated to 180 °C for 24 h. The resulting suspension was centrifuged, and the solids were washed several times with deionized water and once with absolute ethanol (Panreac). All the obtained powders were dried at 80 °C for 24 h.

3.2. Physical, Compositional, and Redox Characterization

XRD patterns were recorded on a D8 ADVANCE diffractometer (Bruker, Karlsruhe, Germany) using $\text{Cu K}\alpha$ radiation, with a range of 5°–110°, a step of 0.02°, and a step time of 1 s. The average crystal size of samples was calculated using the Scherrer equation through the width of the {111} diffraction peak of ceria measured by the software DiffractPlus.

ICP analysis was performed using an ICP-AES Iris Intrepid instrument (Thermal Elemental, Franklin, MA, USA).

In order to measure the specific Brunauer–Emmett–Teller (BET) surface areas of all samples, N_2 physisorption was carried out in a Micromeritics ASAP 2020 at –196 °C. The samples were previously degasified at 150 °C for 2 h under vacuum.

Transmission and scanning transmission electron microscopy (TEM-STEM) techniques were performed using a JEOL 2010-F (Tokyo, Japan) electron microscope with 0.19 nm spatial resolution at Scherzer defocus. High-angle annular dark-field scanning transmission electron microscopy images (HAADF-STEM) were obtained by using an electron probe of 0.5 nm diameter at a camera length of 8 cm, combined with an EDX system to analyze chemical compositions at different positions.

Redox properties were examined using H_2 -TPR and OSC measurements). Samples were pretreated in an oxidizing atmosphere of 5% O_2 /He flow (60 mL/min) at 500 °C for 1 h prior to both measurements. The samples were cooled in the same oxidizing flow down to 150 °C and kept at this temperature for 30 min, in the case of the OSC measurements; for H_2 -TPR analysis, the flow was switched to pure helium gas, and then samples were cooled down to room temperature. In H_2 -TPR analysis, samples were heated at a rate of 10 °C/min to 950 °C, keeping this final temperature for 1 h in a reducing flow of 5% H_2 /Ar (60 mL/min). Mass/charge ratios (m/z : 2 and 18, H_2 consumption and H_2O formation, respectively) were measured using a Thermostat GSD301T1 mass spectrometer (Pfeiffer Vacuum, Asslar, Germany). In the case of the OSC measurements, the analyses were carried out via a thermogravimetric system, using a SDT Q600 horizontal thermobalance (TA Instruments, New Castle, DE, USA). The measurements consisted of the monitoring of the weight loss of each sample under a 60 mL/min flow of 5% H_2 /Ar, at isothermal steady state for 1 h. Weight losses were measured at 200, 350, 500, and 700 °C. In all cases, samples were heated at a rate of 10 °C/min. The amount of Ce^{3+} generated was calculated based on the total weight loss of the sample, which was only due to the evolution of lattice oxygen.

3.3. Catalytic Test: NO Oxidation to NO₂

The catalytic tests consisted of temperature-programmed oxidations, where the temperature was increased from room temperature up to 700 °C at 10 °C/min under the reactive atmosphere, with the purpose of quantifying the NO to NO₂ oxidation capacity of the catalysts. The total flow used was 500 mL/min (GHSV 30,000 h⁻¹), and the gas composition was 500 ppm NO, 5%O₂, and N₂ balance. The gas went through 80 mg of sample, mixed with 300 mg of SiC, and was deposited in a fixed-bed reactor. The reaction was monitored using specific NDIR-UV gas analyzers (Rosemount Analytical, Fisher-Rosemount, Hasselroth, Germany). The analyzed gases were NO, NO₂, and O₂.

NO_x elimination curves were also obtained from 100 °C to 700 °C by comparison with the NO_x profiles obtained in a “blank” experiment (only with SiC).

4. Conclusions

Pure and lanthanum-doped (5, 10, and 15 mol.%) ceria samples with controlled morphology were synthesized under hydrothermal conditions. The solubility limit of lanthanum in CeO₂ nanocubes was estimated to be 10 at.%, as the catalyst prepared with 15 mol.% of lanthanum presented a mixture of morphologies (nanocubes and nanorods). X-EDS analyses confirmed that these nanorods exhibited a composition richer in lanthanum than their nanocube counterparts.

In general, increasing the amount of lanthanum incorporated into the cerium oxide structure enhanced sample reducibility. However, the trend in catalytic activity for NO oxidation did not totally adhere to the redox behavior tendency, as the most active sample, Ce_{0.90}O_{0.10}O_{2-δ}, is not the most reducible one. This result highlighted the importance of nanoparticle morphology in NO oxidation, as lanthanum-rich nanorods seem to favor the formation of quite stable N-chemisorbed species and the formation of hydroxycarbonates, which could act against NO oxidation. Ultimately, the most active sample was Ce_{0.90}O_{0.10}O_{2-δ}, whose particles presented a uniform nanocube shape and exhibited an improved redox behavior with respect to ceria and Ce_{0.95}O_{0.05}O_{2-δ}, being the most reducible catalyst among those presenting the “suitable” unique morphology.

Further research on the following areas will help to move forward on the understanding of the impact and relevance of various parameters affecting the properties and practical applications of La-ceria nanoparticles for the NO oxidation reaction:

- Investigating the reaction mechanism of NO adsorption and oxidation over La-doped ceria catalysts using in situ diffuse reflectance infrared Fourier transform spectroscopy (in situ DRIFTS);
- Evaluating the catalytic activity of the most active La-ceria catalysts towards NO oxidation under a more real composition of the exhaust gas, analyzing the impact of the presence of CO₂, hydrocarbons, and H₂O on the catalysts' performances.

Supplementary Materials: The following supporting information can be downloaded at <https://www.mdpi.com/article/10.3390/catal13050894/s1>, Figure S1: HRTEM images of (a) CeO₂ NC, (b) Ce_{0.95}La_{0.05}O_{2-δ} NC, (c) Ce_{0.90}La_{0.10}O_{2-δ} NC, and (d) Ce_{0.85}La_{0.15}O_{2-δ} NC+NR. Digital diffraction patterns, which are displayed at the bottom left corner of each image, have been acquired at the different areas enclosed in white. All scale bars correspond to 10 nm; Figure S2: TEM image of La(OH)₃ sample, presenting a nanorod morphology; Figure S3: XRD diffractogram of La(OH)₃ sample compared with a lanthanum hydroxide reference pattern [64]; Figure S4: NO₂ production of Ce_{1-x}La_xO_{2-δ} (x: 0, 5, 10, and 15 mol.%) (nanocubes/nanorods) and La(OH)₃ NR versus calculated/theoretical curves, represented by dotted lines.

Author Contributions: S.F.-G. and A.G.-G.: conceptualization; S.F.-G., J.G.-M., J.C.M.-M. and M.T.: methodology; S.F.-G., M.T. and A.G.-G.: formal analysis; S.F.-G., M.T., J.G.-M. and A.G.-G.: investigation; S.F.-G.: writing—original draft preparation; M.T. and A.G.-G.: writing—review and editing; A.B.H., X.C. and J.J.C.: supervision; J.J.C. and A.G.-G.: funding acquisition. All authors have read and agreed to the published version of the manuscript.

Funding: This research was funded by Generalitat Valenciana (CIPROM/2021/070 project), the Spanish Ministry of Science and Innovation/Research Spanish Agency (PID2019-105542RB-I00/AEI/10.13039/501100011033, PID2020-113006RB-I00/AEI/10.13039/501100011033 and PID2020-113809RB-C33 projects), and UE-FEDER funding.

Data Availability Statement: Not applicable.

Acknowledgments: M.T. thanks the FPU scholarship program of the Ministry of Education for financial support. J.C.M.-M. acknowledges the Spanish Ministry of Science and Innovation for financial support through an FPU grant (FPU17/00603).

Conflicts of Interest: The authors declare no conflict of interest.

References

1. Han, L.; Cai, S.; Gao, M.; Hasegawa, J.; Wang, P.; Zhang, J.; Shi, L.; Zhang, D. Selective catalytic reduction of NO_x with NH₃ by using novel catalysts: State of the art and future prospects. *Chem. Rev.* **2019**, *119*, 10916–10976. [[CrossRef](#)] [[PubMed](#)]
2. Chen, L.; Zhang, C.; Wu, T.; Huang, B.; Zhang, J.; Guan, G.; Zhang, Z.; Hou, X.; Hu, C.; Lu, Q. Effects of a-site replacement (Sm, Y, and Pr) on catalytic performances of mullite catalysts for NO oxidation. *Fuel* **2023**, *337*, 126838. [[CrossRef](#)]
3. Zhang, T.; Li, H.; Yang, Z.; Cao, F.; Li, L.; Chen, H.; Liu, H.; Xiong, K.; Wu, J.; Hong, Z.; et al. Electrospun YMn₂O₅ nanofibers: A highly catalytic activity for NO oxidation. *Appl. Catal. B* **2019**, *247*, 133–141. [[CrossRef](#)]
4. Jiang, X.-Q.; Mei, X.-D.; Feng, D. Air pollution and chronic airway diseases: What should people know and do? *J. Thorac. Dis.* **2016**, *8*, E31.
5. Ma, S.-j.; Wang, X.-w.; Chen, T.; Yuan, Z.H. Effect of surface morphology on catalytic activity for NO Oxidation of SmMn₂O₅ nanocrystals. *Chem. Eng. J.* **2018**, *354*, 191–196. [[CrossRef](#)]
6. France, L.J.; Yang, Q.; Li, W.; Chen, Z.; Guang, J.; Guo, D.; Wang, L.; Li, X. Ceria Modified FeMnO_x—Enhanced performance and sulphur resistance for low-temperature SCR of NO_x. *Appl. Catal. B* **2017**, *206*, 203–215. [[CrossRef](#)]
7. Atribak, I.; Bueno-López, A.; García-García, A. Combined removal of diesel soot particulates and NO_x over CeO₂–ZrO₂ mixed oxides. *J. Catal.* **2008**, *259*, 123–132. [[CrossRef](#)]
8. Atribak, I.; Bueno-López, A.; García-García, A.; Azambre, B. Contributions of surface and bulk heterogeneities to the NO oxidation activities of ceria–zirconia catalysts with composition Ce_{0.76}Zr_{0.24}O₂ prepared by different methods. *Phys. Chem. Chem. Phys.* **2010**, *12*, 13770–13779. [[CrossRef](#)]
9. Yang, N.; Yu, J.L.; Dou, J.X.; Tahmasebi, A.; Song, H.; Moghtaderi, B.; Lucas, J.; Wall, T. The effects of oxygen and metal oxide catalysts on the reduction reaction of NO with lignite char during combustion flue gas cleaning. *Fuel Process. Technol.* **2016**, *152*, 102–107. [[CrossRef](#)]
10. Ali, S.; Chen, L.; Yuan, F.; Li, R.; Zhang, T.; Bakhtiar, S.H.; Leng, X.; Niu, X.; Zhu, Y. Synergistic effect between copper and cerium on the performance of Cu_x-Ce_{0.5-x}-Zr_{0.5} (x = 0.1–0.5) oxides catalysts for selective catalytic reduction of NO with ammonia. *Appl. Catal. B* **2017**, *210*, 223–234. [[CrossRef](#)]
11. Song, I.; Youn, S.; Lee, H.; Lee, S.G.; Cho, S.J.; Kim, D.H. Effects of Microporous TiO₂ support on the catalytic and structural properties of V₂O₅/Microporous TiO₂ for the selective catalytic reduction of NO by NH₃. *Appl. Catal. B* **2017**, *210*, 421–431. [[CrossRef](#)]
12. Auvray, X.; Olsson, L. Stability and activity of Pd-, Pt- and Pd–Pt catalysts supported on alumina for NO oxidation. *Appl. Catal. B* **2015**, *168–169*, 342–352. [[CrossRef](#)]
13. Li, L.; Qu, L.; Cheng, J.; Li, J.; Hao, Z. Oxidation of nitric oxide to nitrogen dioxide over Ru catalysts. *Appl. Catal. B* **2009**, *88*, 224–231. [[CrossRef](#)]
14. Wang, X.; Liu, D.; Song, S.; Zhang, H. Pt@CeO₂ multicore@Shell self-assembled nanospheres: Clean synthesis, structure optimization, and catalytic applications. *J. Am. Chem. Soc.* **2013**, *135*, 15864–15872. [[CrossRef](#)]
15. Liu, C.; Shi, J.-W.; Gao, C.; Niu, C. Manganese oxide-based catalysts for low-temperature selective catalytic reduction of NO_x with NH₃: A Review. *Appl. Catal. A Gen.* **2016**, *522*, 54–69. [[CrossRef](#)]
16. Trovarelli, A. *Catalysis by Ceria and Related Materials*; World Scientific: Singapore, 2002; Volume 2, ISBN 1783261315.
17. Zhu, Y.; Li, C.; Liang, C.; Li, S.; Liu, X.; Du, X.; Yang, K.; Zhao, J.; Yu, Q.; Zhai, Y.; et al. Regulating CeO₂ morphologies on the catalytic oxidation of toluene at lower temperature: A study of the structure–activity relationship. *J. Catal.* **2023**, *418*, 151–162. [[CrossRef](#)]
18. Wu, Z.; Li, M.; Overbury, S.H. On the structure dependence of CO oxidation over CeO₂ nanocrystals with well-defined surface planes. *J. Catal.* **2012**, *285*, 61–73. [[CrossRef](#)]
19. Aneggi, E.; Wiater, D.; de Leitenburg, C.; Llorca, J.; Trovarelli, A. Shape-dependent activity of ceria in soot combustion. *ACS Catal.* **2013**, *4*, 172–181. [[CrossRef](#)]
20. Gao, R.; Zhang, D.; Maitarad, P.; Shi, L.; Rungrotmongkol, T.; Li, H.; Zhang, J.; Cao, W. Morphology-dependent properties of MnO_x/ZrO₂–CeO₂ Nanostructures for the selective catalytic reduction of NO with NH₃. *J. Phys. Chem. C* **2013**, *117*, 10502–10511. [[CrossRef](#)]

21. Tinoco, M.; Fernandez-Garcia, S.; Villa, A.; Gonzalez, J.M.; Blanco, G.; Hungria, A.B.; Jiang, L.; Prati, L.; Calvino, J.J.; Chen, X. Selective oxidation of glycerol on morphology controlled ceria nanomaterials. *Catal. Sci. Technol.* **2019**, *9*, 2328–2334. [[CrossRef](#)]
22. Ouyang, B.; Tan, W.; Liu, B. Morphology effect of nanostructure ceria on the Cu/CeO₂ catalysts for synthesis of methanol from CO₂ hydrogenation. *Catal. Commun.* **2017**, *95*, 36–39. [[CrossRef](#)]
23. Tina; Zhang, M.; Li, J.; Li, H.; Li, Y.; Shen, W. Morphology-dependent redox and catalytic properties of CeO₂ nanostructures: Nanowires, nanorods and nanoparticles. *Catal. Today* **2009**, *148*, 179–183.
24. Zhou, K.; Wang, X.; Sun, X.; Peng, Q.; Li, Y. Enhanced catalytic activity of ceria nanorods from well-defined reactive crystal planes. *J. Catal.* **2005**, *229*, 206–212. [[CrossRef](#)]
25. Qiao, Z.-A.; Wu, Z.; Dai, S. Shape-controlled ceria-based nanostructures for catalysis applications. *ChemSusChem* **2013**, *6*, 1821–1833. [[CrossRef](#)]
26. Mai, H.-X.; Sun, L.-D.; Zhang, Y.-W.; Si, R.; Feng, W.; Zhang, H.-P.; Liu, H.-C.; Yan, C.-H. Shape-selective synthesis and oxygen storage behavior of ceria nanopolyhedra, nanorods, and nanocubes. *J. Phys. Chem. B* **2005**, *109*, 24380–24385. [[CrossRef](#)] [[PubMed](#)]
27. Di Sarli, V.; Landi, G.; Di Benedetto, A.; Lisi, L. Synergy between ceria and metals (Ag or Cu) in catalytic diesel particulate filters: Effect of the metal content and of the preparation method on the regeneration performance. *Top. Catal.* **2021**, *64*, 256–269. [[CrossRef](#)]
28. Yeste, M.P.; Primus, P.A.; Alcantara, R.; Cauqui, M.A.; Calvino, J.J.; Pintado, J.M.; Blanco, G. Surface Characterization of Two Ce_{0.6}Zr_{0.3}O₂ Mixed Oxides with Different Reducibility. *Appl. Surf. Sci.* **2020**, *503*, 144255. [[CrossRef](#)]
29. Mamontov, E.; Brezny, R.; Koranne, M.; Egami, T. Nanoscale heterogeneities and oxygen storage capacity of Ce_{0.5}Zr_{0.5}O₂. *J. Phys. Chem. B* **2003**, *107*, 13007–13014. [[CrossRef](#)]
30. Bernal, S.; Blanco, G.; Cauqui, M.A.; Cifredo, G.A.; Pintado, J.M.; Rodriguez-Izquierdo, J.M. Influence of reduction treatment on the structural and redox behaviour of ceria, La/Ce and Y/Ce mixed oxides. *Catal. Lett.* **1998**, *53*, 51–57. [[CrossRef](#)]
31. Hernández, W.Y.; Laguna, O.H.; Centeno, M.A.; Odriozola, J.A. Structural and catalytic properties of lanthanide (La, Eu, Gd) doped ceria. *J. Solid State Chem.* **2011**, *184*, 3014–3020. [[CrossRef](#)]
32. Giménez-Mañogil, J.; Guillén-Hurtado, N.; Fernández-García, S.; Chen, X.; Calvino-Gámez, J.J.; García-García, A. Ceria-Praseodymia mixed oxides: Relationships between redox properties and catalytic activities towards NO oxidation to NO₂ and CO-PROX reactions. *Top. Catal.* **2016**, *59*, 1065–1070. [[CrossRef](#)]
33. Bernal, S.; Blanco, G.; Cauqui, M.A.; Corchado, P.; Pintado, J.M.; Rodríguez-Izquierdo, J.M. Oxygen buffering capacity of mixed cerium terbium oxide: A new material with potential applications in three-way catalysts. *Chem. Commun.* **1997**, *16*, 1545–1546. [[CrossRef](#)]
34. Bueno-López, A. Diesel soot combustion ceria catalysts. *Appl. Catal. B* **2014**, *146*, 1–11. [[CrossRef](#)]
35. Trindade, F.J.; Damasceno, S.; Otubo, L.; Felez, M.R.; De Florio, D.Z.; Fonseca, F.C.; Ferlauto, A.S. Tuning of shape, defects, and disorder in lanthanum-doped ceria nanoparticles: Implications for high-temperature catalysis. *ACS Appl. Nano Mater.* **2022**, *5*, 8859–8867. [[CrossRef](#)]
36. Xia, X.; Li, J.; Chen, C.; Lan, Y.-P.; Mao, X.; Chu, Z.; Ning, D.; Zhang, J.; Liu, F. Collaborative influence of morphology tuning and RE (La, Y, and Sm) doping on photocatalytic performance of nanoceria. *Environ. Sci. Pollut. Res.* **2022**, *29*, 88866–88881. [[CrossRef](#)] [[PubMed](#)]
37. Xia, X.; Li, J.; Chen, C.; Lan, Y.-P.; Mao, X.; Bai, F. Optimal rare-earth (La, Y and Sm) doping conditions and enhanced mechanism for photocatalytic application of ceria nanorods. *Nanotechnology* **2021**, *32*, 195708. [[CrossRef](#)] [[PubMed](#)]
38. Sartoretti, E.; Novara, C.; Chiodoni, A.; Giorgis, F.; Piumetti, M.; Bensaid, S.; Russo, N.; Fino, D. Nanostructured ceria-based catalysts doped with La and Nd: How acid-base sites and redox properties determine the oxidation mechanisms. *Catal. Today* **2022**, *390–391*, 117–134. [[CrossRef](#)]
39. Mohanty, B.; Nayak, J. Parameters dependent studies of structural, optical and electrical properties of CeO₂ nanoparticles prepared via facile one-pot hydrothermal technique. *Mater. Res. Express* **2017**, *4*, 115015. [[CrossRef](#)]
40. Loche, D.; Morgan, L.M.; Casu, A.; Mountjoy, G.; O'Regan, C.; Corrias, A.; Falqui, A. Determining the maximum lanthanum incorporation in the fluorite structure of La-doped ceria nanocubes for enhanced redox ability. *RSC Adv.* **2019**, *9*, 6745–6751. [[CrossRef](#)]
41. Fernandez-Garcia, S.; Jiang, L.; Tinoco, M.; Hungria, A.B.; Han, J.; Blanco, G.; Calvino, J.J.; Chen, X. Enhanced hydroxyl radical scavenging activity by doping lanthanum in ceria nanocubes. *J. Phys. Chem. C* **2016**, *120*, 1891–1901. [[CrossRef](#)]
42. Dean, J.A. *Lange's Handbook of Chemistry*; McGraw-Hill: New York, NY, USA, 1985; Volume 13.
43. Ryan, K.; McGrath, J.; Farrell, R.; O'Neill, W.; Barnes, C.; Morris, M. Measurements of the lattice constant of Ceria when doped with lanthana and praseodymia-The possibility of local defect ordering and the observation of extensive phase separation. *J. Phys. Condens. Matter* **2003**, *15*, L49. [[CrossRef](#)]
44. Liang, S.; Vesper, G. Mixed lanthana/ceria nanorod-supported gold catalysts for water–gas-shift. *Catal. Lett.* **2012**, *142*, 936–945. [[CrossRef](#)]
45. Deng, W.; Frenkel, A.I.; Si, R.; Flytzani-Stephanopoulos, M. Reaction-relevant gold structures in the low temperature water-gas shift Reaction on Au-CeO₂. *J. Phys. Chem. C* **2008**, *112*, 12834–12840. [[CrossRef](#)]
46. Sudarsanam, P.; Mallesham, B.; Reddy, P.S.; Großmann, D.; Grünert, W.; Reddy, B.M. Nano-Au/CeO₂ catalysts for CO oxidation: Influence of dopants (Fe, La and Zr) on the physicochemical properties and catalytic activity. *Appl. Catal. B* **2014**, *144*, 900–908. [[CrossRef](#)]

47. Jiang, L.; Fernandez-Garcia, S.; Tinoco, M.; Yan, Z.; Xue, Q.; Blanco, G.; Calvino, J.J.; Hungria, A.B.; Chen, X. Improved oxidase mimetic activity by praseodymium incorporation into ceria nanocubes. *ACS Appl. Mater. Interfaces* **2017**, *9*, 18595–18608. [[CrossRef](#)]
48. Biswas, M.; Bandyopadhyay, S. Synthesis of La³⁺ doped nanocrystalline ceria powder by urea–formaldehyde gel combustion route. *Mater. Res. Bull.* **2012**, *47*, 544–550. [[CrossRef](#)]
49. Kašpar, J.; Fornasiero, P.; Graziani, M. Use of CeO₂-based oxides in the three-way catalysis. *Catal. Today* **1999**, *50*, 285–298. [[CrossRef](#)]
50. Johnson, M.F.L.; Mooi, J. Cerium dioxide crystallite sizes by temperature-programmed reduction. *J. Catal.* **1987**, *103*, 502–505. [[CrossRef](#)]
51. Giordano, F.; Trovarelli, A.; De Leitenburg, C.; Giona, M. A model for the temperature-programmed reduction of low and high surface area ceria. *J. Catal.* **2000**, *193*, 273–282. [[CrossRef](#)]
52. Boaro, M.; Vicario, M.; De Leitenburg, C.; Dolcetti, G.; Trovarelli, A. The use of temperature-programmed and dynamic/transient methods in catalysis: Characterization of ceria-based, model three-way catalysts. *Catal. Today* **2003**, *77*, 407–417. [[CrossRef](#)]
53. Désaunay, T.; Bonura, G.; Chiodo, V.; Freni, S.; Couzinié, J.P.; Bourgon, J.; Ringuedé, A.; Labat, F.; Adamo, C.; Cassir, M. Surface-dependent oxidation of H₂ on CeO₂ surfaces. *J. Catal.* **2013**, *297*, 193–201. [[CrossRef](#)]
54. Tsunekawa, S.; Sivamohan, R.; Ito, S.; Kasuya, A.; Fukuda, T. Structural study on monosize CeO_{2-x} nano-particles. *Nanostruct. Mater.* **1999**, *11*, 141–147. [[CrossRef](#)]
55. Yao, H.C.; Yao, Y.F.Y. Ceria in automotive exhaust catalysts: I. Oxygen storage. *J. Catal.* **1984**, *86*, 254–265. [[CrossRef](#)]
56. Deganello, F.; Martorana, A. Phase analysis and oxygen storage capacity of ceria-lanthana-based TWC promoters prepared by sol–gel routes. *J. Solid State Chem.* **2002**, *163*, 527–533. [[CrossRef](#)]
57. Bray, J.M.; Schneider, W.F. First-principles analysis of structure sensitivity in NO oxidation on Pt. *ACS Catal.* **2015**, *5*, 1087–1099. [[CrossRef](#)]
58. Guillén-Hurtado, N.; Atribak, I.; Bueno-López, A.; García-García, A. Influence of the cerium precursor on the physico-chemical features and NO to NO₂ oxidation activity of ceria and ceria–zirconia catalysts. *J. Mol. Catal. A Chem.* **2010**, *323*, 52–58. [[CrossRef](#)]
59. Atribak, I.; Azambre, B.; Bueno López, A.; García-García, A. Effect of NO_x adsorption/desorption over ceria-zirconia catalysts on the catalytic combustion of model soot. *Appl. Catal. B* **2009**, *92*, 126–137. [[CrossRef](#)]
60. Azambre, B.; Atribak, I.; Bueno-López, A.; García-García, A. Probing the surface of ceria–zirconia catalysts using NO_x adsorption/desorption: A first step toward the investigation of crystallite heterogeneity. *J. Phys. Chem. C* **2010**, *114*, 13300–13312. [[CrossRef](#)]
61. Klingenberg, B.; Vannice, M.A. Influence of pretreatment on lanthanum nitrate, carbonate, and oxide powders. *Chem. Mater.* **1996**, *8*, 2755–2768. [[CrossRef](#)]
62. Zhang, B.; Li, D.; Wang, X. Catalytic performance of La–Ce–O mixed oxide for combustion of methane. *Catal. Today* **2010**, *158*, 348–353. [[CrossRef](#)]
63. Nolan, M. Molecular adsorption on the doped (110) ceria surface. *J. Phys. Chem. C* **2009**, *113*, 2425–2432. [[CrossRef](#)]
64. Djerdj, I.; Garnweitner, G.; Sheng Su, D.; Niederberger, M. Morphology-controlled nonaqueous synthesis of anisotropic lanthanum hydroxide nanoparticles. *J. Solid State Chem.* **2007**, *180*, 2154–2165. [[CrossRef](#)]

Disclaimer/Publisher’s Note: The statements, opinions and data contained in all publications are solely those of the individual author(s) and contributor(s) and not of MDPI and/or the editor(s). MDPI and/or the editor(s) disclaim responsibility for any injury to people or property resulting from any ideas, methods, instructions or products referred to in the content.